Intermediate valence and spin fluctuations near a quantum critical point in CeRu$_{2-x}$Co$_x$Ge$_2$

Swati Pandey [1,2,*] Ashish Kumar Mishra [3] M. P. Saravanan [3] P. K. Biswas,[4,†] A. K. Yadav [5] S. N. Jha [5]
D. Bhattacharyya,[5] R. J. Choudhary,[3] R. Rawat [3] and V. Siruguri [1]

[1]*UGC-DAE Consortium for Scientific Research Mumbai Centre, BARC Campus, Mumbai 400085, India*
[2]*Department of Physics, Indian Institute of Technology Kanpur, Kanpur 208016, India*
[3]*UGC-DAE Consortium for Scientific Research, University Campus, Khandwa Road, Indore 452001, India*
[4]*ISIS Facility, Rutherford Appleton Laboratory, Chilton, Didcot, Oxfordshire OX11 0QX, United Kingdom*
[5]*Atomic and Molecular Physics Division, BARC, Mumbai 400085, India*

We show the presence of a quantum critical point in CeRu$_{2-x}$Co$_x$Ge$_2$ ($0 \leqslant x \leqslant 2$) using detailed heat capacity and muon spin relaxation (μSR) measurements. The millikelvin heat capacity and μSR results for the critical composition $x_C \sim 1.5$ are consistent with the spin fluctuation model of the quantum critical point. The time-field-temperature scaling of the heat capacity and μSR data further suggests the role of critical and cooperative spin fluctuations near the antiferromagnetic quantum critical point. In addition, the temperature-dependent x-ray absorption near edge structure reveals intermediate valence fluctuation down to the lowest temperature for the compositions $x \geqslant 1.5$. The noninteger valence for the critical composition $x_C \sim 1.5$ is further demonstrated by room temperature x-ray photoelectron spectroscopy. Interestingly, the quantum criticality in CeRu$_{2-x}$Co$_x$Ge$_2$ is governed by the survival of valence and spin fluctuations down to the lowest temperature.

I. INTRODUCTION

Ce$T_2 X_2$ (T: transition metal; X: Si or Ge) intermetallic compounds provide a wealth of interesting phenomena and diverse ground states such as Kondo effect, heavy fermion behavior, intermediate valence fluctuation (IVF), quantum criticality, and unconventional superconductivity [1–7]. These phenomena arise due to the instability of $4f$ electrons, which results in a high density of states near the Fermi level. Based on the Doniach model [8], the competing long-range magnetic ordering mediated by the Ruderman-Kittel-Kasuya-Yosida (RKKY) interaction and the on-site Kondo interaction between $4f$ and conduction electrons in these systems leads to a quantum critical point (QCP) [9]. A quantum phase transition (QPT), separating the magnetic and nonmagnetic phases, occurs at $T = 0$ K via some nonthermal parameter such as pressure (p), magnetic field (H), and chemical substitution (x) and forms a central topic in the study of strongly correlated electron systems [10–13].

Further, a nearby QPT in the T-x or p-T phase diagram results in non-Fermi liquid (nFL) behavior in the physical and thermodynamical properties, where electrical resistivity (ρ), heat capacity (C), and magnetic susceptibility (χ) deviate from $\rho(T) \sim T^2$, $C(T)/T \sim \gamma_0$ (Sommerfeld coefficient), and $\chi(T) \sim$ constant, behavior. The spin fluctuation theory of Moriya successfully describes the nFL behavior in many $3d$ electron systems near a magnetic to nonmagnetic phase transition at $T = 0$ K [14]. However, with a few exceptions, it fails to explain the results of various $4f$ electron systems

[15]. Nevertheless, different theoretical approaches have been employed to understand the breakdown of the Landau Fermi liquid theory in $4f$ metals near a QPT, like the disordered Kondo model [16], the quantum Griffiths model [17], valence fluctuation (VF) [18], and local criticality [19].

The description of QPT based on the IVF model in Ce and Yb systems [20–23] has recently sparked the curiosity of experimental and theoretical works, as the Ce $4f$ electron is on the verge of exhibiting either the localized or itinerant character. In Ce-based systems, the $4f$ shell has single electron occupancy, and the strong hybridization between $4f$ and conduction electrons results in a decrease in the $4f$ localization. This further causes the deviation of the average Ce valence from $3+$ and leads to the intermediate valence state, where the electrons are exchanged between $4f$ level and conduction electrons, fluctuating between the $4f^1(5d6s)^3 \leftrightarrow 4f^0(5d6s)^4$ configurations. Since the energy difference between Ce$^{+3}(4f^1)$ and Ce$^{+4}(4f^0)$ ground state configurations is small, valence fluctuations are common in Ce and Yb compounds [24,25]. Importantly, these valence fluctuations near quantum criticality are suggested as a pairing mechanism for the superconductivity observed in CeCu$_2$Ge$_2$, CeCu$_2$Si$_2$, and YbAlB$_4$ as a function of pressure [26–29].

The intermetallic series CeRu$_{2-x}$Co$_x$Ge$_2$ is an excellent choice for tuning hybridization strength as the valence of the Ce ion changes from trivalent (for $x = 0$) to valence fluctuating (for $x = 2$) [4]. In this series, CeRu$_2$Ge$_2$ exhibits two successive magnetic transitions from paramagnetic to antiferromagnetic (PM-AFM) at $T_N = 8.5$ K and $T_C = 7.4$ K from antiferromagnetic to ferromagnetic (AFM-FM), whereas CeCo$_2$Ge$_2$ is an IVF compound [5,30–33]. Nevertheless, our recent findings in CeRu$_{2-x}$Co$_x$Ge$_2$ ($0 \leqslant x \leqslant 2$) [4,5], based on heat capacity, electrical resistivity, and

*pswati@iitk.ac.in
†Deceased.

magnetization results, suggested an IVF-induced QCP in the T-x phase diagram at a critical concentration $x_C \sim 1.5$, resulting in the instability of the $4f$ electron in compounds with $x \geqslant 1.5$. However, the results were limited to minimum temperature of 2 K, at which the C/T versus T curve continues to show a logarithmic rise with a decrease in temperature for the critical composition. In this paper, we investigate the nature of QCP down to millikelvin range using heat capacity and the muon spin relaxation (μSR) technique, which probes the presence of magnetic order on macroscopic and microscopic length scales, respectively. Since the magnetic moments near a QCP are usually small and unstable, μSR is an excellent tool to gain a microscopic insight of the spin dynamics in this neighborhood [34–36]. To investigate the valence fluctuation, the temperature-dependent Ce L_{III} edge x-ray absorption near edge structure (XANES) and x-ray photoelectron spectroscopy (XPS) measurements were used. Based on this experimental evidence, we argue that the valence fluctuations compete with spin fluctuations in CeRu$_{2-x}$Co$_x$Ge$_2$ down to the lowest temperatures.

The Ce L_{III} edge XANES results of CeRu$_2$Ge$_2$, CeRu$_{0.5}$Co$_{1.5}$Ge$_2$, and CeCo$_2$Ge$_2$ are described in Sec. III A, Ce $3d$ core XPS is presented in Sec. III B, heat capacity results are presented in Sec. III C, μSR results are presented in Sec. III D, and Sec. III E describes the scaling analysis.

II. EXPERIMENTAL DETAILS

Polycrystalline samples of CeRu$_{2-x}$Co$_x$Ge$_2$ ($0 \leqslant x \leqslant 2$) were prepared using the arc melting technique as described in Ref. [5]. The valence state of Ce was determined using XANES, performed in the temperature range 300–12 K. The XANES measurements were carried out at the energy-scanning EXAFS beamline (BL-9) at the Indus-2 Synchrotron Source (2.5 GeV, 100 mA), RRCAT, Indore [37]. The normalized XANES spectra were obtained using the standard procedure by subtracting the linear baseline below the Ce L_{III} absorption edge and dividing by the absorption edge step. To ensure the reproducibility of the spectra, several absorption scans were collected at each temperature. The x-ray photoelectron spectroscopy (XPS) measurements at room temperature were performed using Al Kα x-ray source (1486.6 eV) with Omicron energy analyzer. The μSR measurements in zero field (ZF) and longitudinal field (LF) were performed using the MuSR spectrometer at the ISIS facility of Rutherford Appleton Laboratory, UK. The powdered sample was mounted on a 99.99% pure silver sample holder using diluted GE varnish and covered with thin silver foil and was cooled down to 50 mK using an Oxford Instruments dilution refrigerator [34]. Heat capacity measurements down to 160 mK and in fields up to 16 T were performed using a dilution refrigerator on a Quantum Design (QD) Physical Property Measurement System (PPMS).

III. RESULTS

A. $x = 0$, 1.5, and 2: Ce L_{III} edge investigations

The XANES technique has found widespread application in determining the rare earth valency and serves as a direct microscopic probe to resolve the ground state configuration

[25,38,39]. Figure 1(a) presents Ce L_{III} XANES spectra of CeRu$_{2-x}$Co$_x$Ge$_2$ ($x = 0$, 1.5, and 2) at 300 K along with the reference sample CeO$_2$. In the L_{III} XANES spectra of Ce-based intermediate valence systems, it is observed that, along with the main absorption peak at 5726 eV, there is the presence of a characteristic maxima similar to CeO$_2$ at around 5737 eV, and the presence of this double peak feature corresponds to ground states of both $4f^1$ and $4f^0$ configurations [40–43]. From the figure, it is clearly evident that the absorption edges of the $x = 1.5$ and 2 samples show characteristics of a mixture of Ce^{+3} and Ce^{+4}, where a strong absorption peak at 5726 eV and a prominent shoulder at 5735 eV, nearly at a similar position to the CeO$_2$ spectra, respectively, belong to the $4f^1$ and $4f^0$ configurations. Nevertheless, an almost flat shoulder with a peak at 5726 eV for $x = 0$ reveals the localized nature of Ce^{+3} ion [24] and suggests a nearly trivalent state of the Ce valence.

Furthermore, to investigate the temperature dependence of Ce valence, we measured XANES spectra for $x = 0$, 1.5, and 2 at different temperatures down to 12 K, as shown in Fig. 1(b), and it clearly shows the survival of the $4f^0$ state down to 12 K for $x = 1.5$ and 2. The Ce L_{III} spectra were analyzed using the conventional fitting procedure as given in Ref. [44]. To estimate the relative populations of the two Ce valence states, the spectrum was deconvoluted into arctangent step functions, which represent the transition from the core to the continuum states, and Gaussian functions, which consider the empty $5d$ states above the Fermi energy. The deconvolution of the $x = 1.5$ spectra at 300 K into two rounded arc tangent functions and two Gaussian functions giving the Ce^{+3} and Ce^{+4} components is shown in Fig. 1(c). The blue line represents the theoretical fit to the data. The valence state of Ce is obtained from the intensity ratio of the two Gaussian curves [marked as A and B in Fig. 1(c)] using the equation $\langle v \rangle = 3 + I_1/(I_1 + I_2)$, where I_1 is the intensity of peak A and I_2 is the intensity of peak B [45–47].

The estimated Ce valence as a function of temperature is shown in Fig. 1(d). For $x = 1.5$ and 2, Ce valence increases with a lowering of temperature, indicating an increase in the Ce^{+4} component. The Ce valence increases from 3.06 to 3.07 for $x = 1.5$ and from 3.07 to 3.09 for $x = 2$, with varying temperatures from 300 to 12 K. Similar orders of valency change are found for other Ce and Yb based compounds [48–50], where the magnitude of the valence change is expected to be of the order of 0.01 due to the moderate strength of U_{fc}, i.e., the Coulomb repulsion between the $4f$ electron at the Ce or Yb site and the conduction electron in comparison to the first-order valence transition with large U_{fc} [51,52]. Moreover, Fig. 1(e) shows Ce valence as a function of increasing Co concentration at 300 K, where the increase in Ce valence is clearly visible for $x \geqslant 1.5$. This change in Ce valence with x is also reflected in the lattice volume [Fig. 1(f)], which decreases with increase in x [5]. The gradual increase in Ce valence with decreasing temperature as well as increasing concentration can be explained by the electronic structure change at the Fermi level as a result of lattice compression and an increase in $4f$-conduction electron hybridization [53,54]. The Ce valence as determined by XANES is consistent with the susceptibility measurement [4] and other Ce intermediate
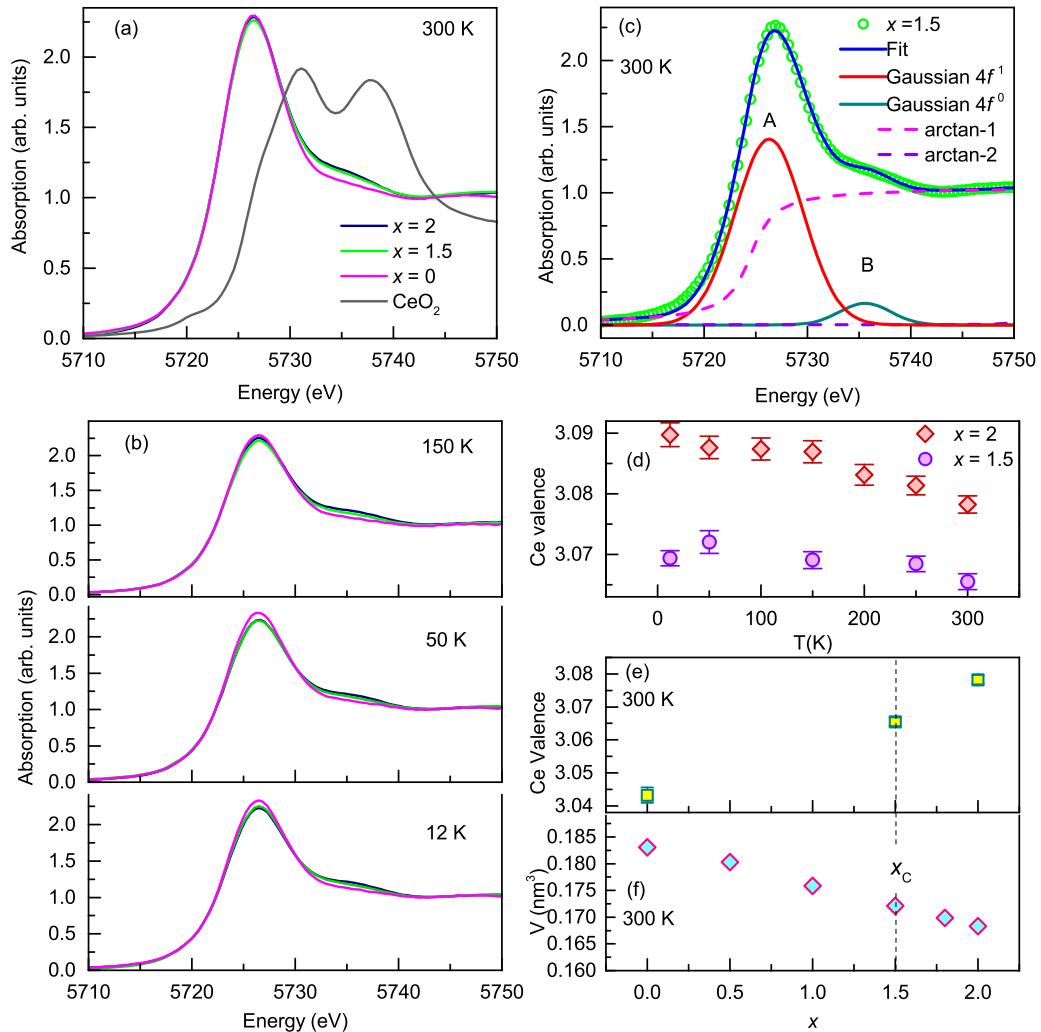
FIG.1. (a) Normalized XANES spectra of CeRu$_{2-x}$Co$_x$Ge$_2$ for $x = 0$, 1.5, and 2 measured at Ce L_{III} edge along with the spectrum for reference CeO$_2$ sample at 300 K. (b) XANES spectra for $x = 0$, 1.5, and 2 at different temperatures. (c) Peak fitting of Ce L_{III} edge XANES for $x = 1.5$ at 300 K. The contributions due to the Ce^{+3}($4f^1$) and Ce^{+4}($4f^0$) configurations are represented by the solid Gaussian lines, while the dashed line represents the arctan functions. (d) Variation of the valence state of Ce as a function of temperature for $x = 1.5$ and 2. (e),(f) Variation of the valence state of Ce and lattice volume [5] as a function of concentration, respectively.

valence compounds [20,55]. To gain more insight into the valence state of Ce ion for $x_C \sim 1.5$ and the hybridization between $4f$ and conduction electron states, we have performed XPS measurements.

B. $x_C = 1.5$: Ce $3d$ XPS

As XPS study of Ce $3d$ core levels provides information regarding the $4f$ shell configurations and the f-conduction electron hybridization, we have studied room temperature Ce $3d$ core level XPS for $x_C \sim 1.5$, as shown in Fig. 2. The deconvolution of the XPS spectrum was done using the Doniach-Šunjic theory [56], and the deconvoluted spectra are shown in the bottom of Fig. 2. In the spectrum, two sets of photoemission lines are observed due to spin-orbit coupling corresponding to the $3d_{3/2}$ and $3d_{5/2}$ states, which are separated by $\Delta_{SO} = 18.6$ eV. Each set consists of three contributions of Ce ion configuration corresponding to f^0, f^1,

and f^2. The component f^1 originates from the screening of the core hole by conduction electrons. In turn, satellite f^2 located at the distance of about 4 eV at the low-energy side from main lines arises due to screening of the core hole by an additional $4f$ electron resulting due to Ce $4f$-conduction electron hybridization. We have observed a pronounced f^2 peak in our spectrum, which indicates that there is a remarkable hybridization between Ce $4f$ states and conduction electron states. The f^0 contribution was observed at a distance of ~ 11 eV from the f^1 peak in the $3d_{5/2}$ component.

Using the calculation model of Gunnarsson and Schönhammer (GS) as described in Refs. [57,58], the hybridization strength (Δ) between $4f$ and conduction electron states as well as the mean occupation of $4f$ levels (n_f) can be determined from the intensity ratios of the particular components $I(f^2)/[I(f^1) + I(f^2)]$ and $I(f^0)/[I(f^0) + I(f^1) + I(f^2)]$, respectively. Using this procedure, we have obtained $\Delta \approx 155$ meV and $n_f \approx 0.94$. This only holds with the assumption
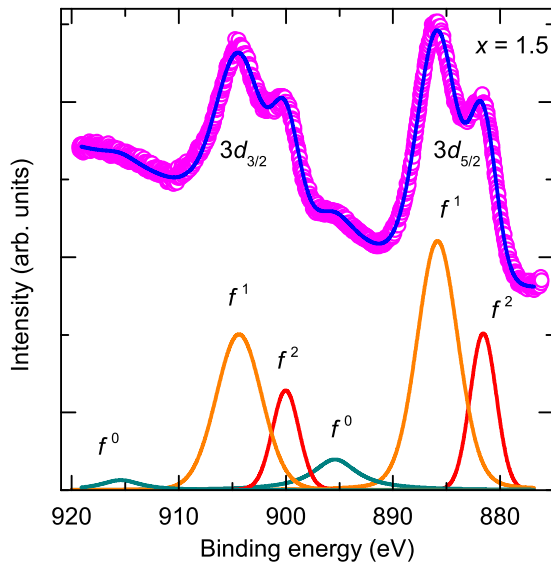
FIG. 2. Ce $3d$ XPS spectra for $x_C \sim 1.5$. The spin orbit split $3d_{3/2}$ and $3d_{5/2}$ components as well as the f^0, f^1, and f^2 contributions are labeled.

that the final state mixing of f^0 and f^1 is minimal provided the large separation ($\sim$11 eV) between them compared to the initial state mixing ($\sim$2 eV), and hence the final state spectral weight of f^0 does not deviate much from the ground state weight for the large Δ. Nevertheless, the estimation of peak intensities ratio, background subtractions, and the approximations involved in GS theory may lead to an error of around 20% in Δ and n_f values [57–60]. The values indicate substantial hybridization for $x_C \sim 1.5$, resulting in delocalization of the $4f$ electrons, which is also reflected in the Ce valence that deviates from Ce^{+3}. The obtained value of Δ is equivalent to other Ce intermediate valence systems [61,62] and is higher than trivalent Ce systems [63,64]. The Ce valence $(3 + \nu) = 3.06$ determined from room temperature XPS measurement agrees with our room temperature XANES result.

C. $x_C = 1.5$: Heat capacity

Figure 3(a) shows zero-field temperature-dependent heat capacity for $x = 0.3$, 0.7, 1.1, and 1.2. A well-separated peak in temperature marks the PM-AFM transition at $T_N \sim 8.3$ K and the AFM-FM transition at $T_C \sim 7.2$ K for $x = 0.3$. T_C is found to decrease with increasing x and move towards the lower temperatures up to $x = 0.7$, beyond which only T_N survives. The variation of T_N follows the Doniach model, where it first increases up to $x = 0.7$, then starts to decrease and vanishes altogether above $x_C \sim 1.5$. The trend of T_N and T_C for the new compositions are consistent with our earlier compositions [4]. In addition, to get a detailed insight into the low-temperature behavior of the critical concentration $x_C \sim 1.5$, we have extended our heat capacity measurement down to 160 mK in different magnetic fields up to 16 T. The low-temperature heat capacity is dominated by the nuclear Schottky contribution, which is evidenced as an upturn in the $C(T)/T$ curve [Fig. 3(b)]. The nuclear Schottky contribution of the form $C_{Sch} \sim \alpha/T^2$ has been subtracted from the heat
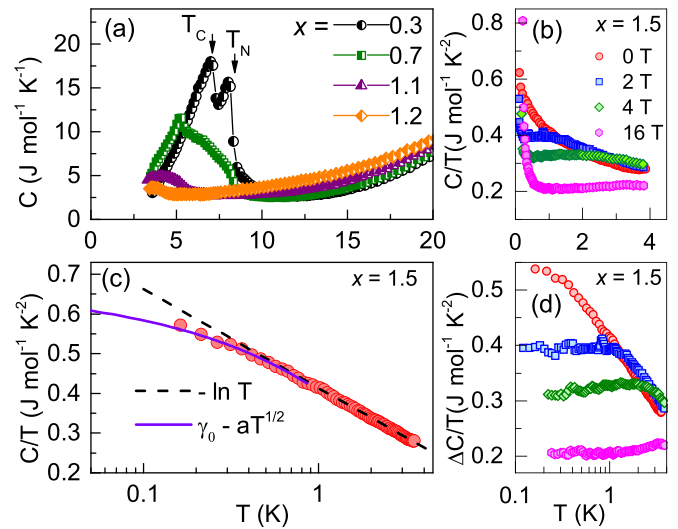

FIG. 3. (a) Temperature-dependent heat capacity for $x = 0.3$, 0.7, 1.1, and 1.2. Arrows mark the transition temperature. (b) C/T vs T for $x_C \sim 1.5$ in the presence of different applied magnetic fields. (c) Semilogarithmic plot of C/T against T for $x_C \sim 1.5$, where the dashed black line and solid violet line represent the logarithmic and power-law dependence, respectively. (d) Semilogarithmic plot of $\Delta C/T$ vs T curve in different magnetic fields.

capacity data [65,66], where the value of α varies between 1.4 and 0.7 $\times$ 10^{-4} J K mol^{-1} as the magnetic field increases from 0 to 16 T. Figure 3(c) shows C/T as a function of temperature on a semilogarithmic scale in a zero magnetic field. The zero-field curve of C/T versus T in Fig. 3(c) does not show any magnetic ordering down to the lowest temperature and follows a negative logarithmic behavior $-\ln T$ for almost a decade in the temperature region between 0.5 and 4 K, consistent with the nFL behavior near a QCP [4]. However, it is interesting to observe that the curve below 0.5 K deviates from the logarithmic behavior and is described by the power law $\sim (\gamma_0 - T^{1/2})$ which is in complete agreement with the spin fluctuation model of Moriya for the 3D AFM case in the weak coupling limit [14,15]. Furthermore, $\Delta C(T)/T$ decreases from its value at $H \sim 0$ T and becomes constant, consistent with crossover to the Fermi liquid state with increasing field [Fig. 3(d)].

D. $x_C = 1.5$: Muon spin relaxation (μSR)

To better understand the low-temperature magnetism of $x_C \sim 1.5$, μSR measurements were performed down to 50 mK. The ZF-μSR asymmetry time spectra obtained at a few selected temperatures between 50 mK and 16 K are shown in Fig. 4. The absence of any oscillations or fast relaxations discards the presence of the static magnetic ordering down to 50 mK. The relaxation spectra are dominated by muon precession in nuclear dipolar fields and are described by the Kubo-Toyabe function. We have analyzed the ZF spectra in the entire temperature range using an exponentially damped relaxation function:

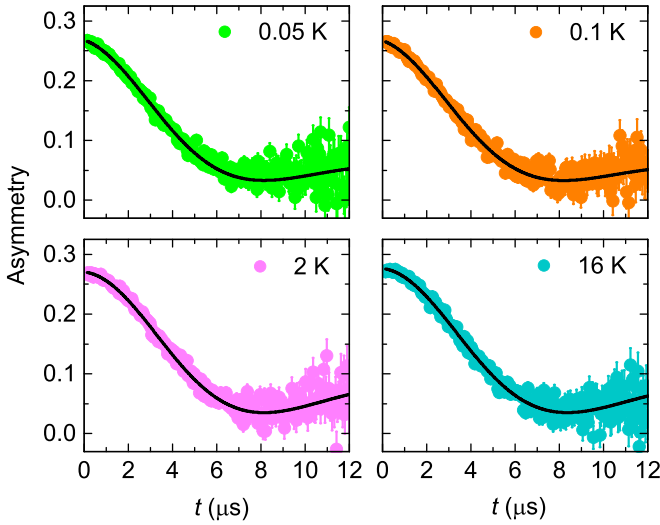$$G_Z(t) = A_0 \, e^{(-\lambda_{ZF} t)} G_{KT}(t) + A_{BG}, \tag{1}$$

FIG. 4. ZF-μSR spectra for $x_C \sim 1.5$ at selected temperatures between 50 mK and 16 K. The solid black lines represent the fits to Eq. (1).
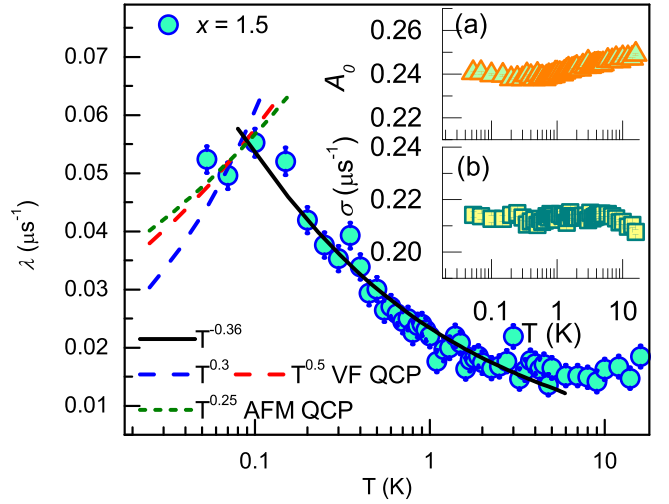

FIG. 5. Semilogarithmic temperature dependencies of parameters obtained from fitting the ZF-μSR spectra for $x_C \sim 1.5$ using Eq. (1). Main panel: temperature dependence of the dynamical relaxation rate (λ_{ZF}). The solid line represents the fit to the power law, $\lambda_{ZF} \sim T^{-n}$. Insets: (a) A_0 and (b) σ versus temperature.

where G_{KT} is the Gaussian Kubo-Toyabe function [67,68] and is given by

$$G_{KT}(t) = \frac{1}{3} + \frac{2}{3}\left(1 - \sigma^2 t^2\right) e^{\left(\frac{-\sigma^2 t^2}{2}\right)}. \qquad (2)$$

Here, A_0 is the initial symmetry at time $t = 0$, σ is the nuclear depolarization rate, σ/γ_μ is the distribution width of the local fields, $\gamma_\mu = 135.53$ MHz/T is the muon gyromagnetic ratio, and λ_{ZF} is the dynamical depolarization rate arising from the fluctuating electronic spins. The background component A_{BG} originating from the muons stopping at the silver sample holder is obtained by fitting the high-temperature spectra and is then fixed for all other temperatures. In Eq. (1), the static Gaussian Kubo-Toyabe function $G_{KT}(t)$ results from a Gaussian distribution of local magnetic fields at the muon site arising from the nuclear spins, while the exponential term $e^{(-\lambda_{ZF}t)}$ is due to the magnetic contribution caused by dynamic magnetic fields associated with fluctuating electronic spins.

Figure 5 presents the temperature dependence of the parameters obtained from the fits of the ZF spectrum with Eq. (1). An almost constant A_0 and σ point towards the absence of long-range ordering down to 50 mK (insets of Fig. 5). Nevertheless, the ZF muon depolarization rate λ_{ZF} (i.e., relaxation rate, $1/T_1$ of μSR) is seen to increase with a decrease in temperature below 2 K, as shown in the main panel of Fig. 5. The increase in λ_{ZF} suggests the slowing down of the critical spin fluctuations associated with a QCP [69]. Below 6 K, λ_{ZF} is found to obey a power law, $\lambda_{ZF} \propto T^{-n}$, with the exponent $n \sim 0.36(1)$, similar to the systems exhibiting QCP [36,70–72]. Furthermore, λ_{ZF} exhibits a cutoff below $T \sim 0.2$ K, which is consistent with the theoretically predicted behavior $\sim T^n$, with an exponent $n \sim 0.3$ for a VF QCP [73]. Similar behavior of λ_{ZF} below $T \sim 0.1$ K in Fe-doped YbAlB$_4$ was attributed to valence criticality [74] and is supported by a recent theoretical study [72]. This further supports our previous conclusion of IVF QCP in CeRu$_{2-x}$Co$_x$Ge$_2$ [4]. Interestingly, the theoretically predicted value for AFM QCP with the exponent $n \sim 0.25$ equally describes the data well below the

cutoff temperature [73]. Both the AFM QCP and the VF QCP suggest the vanishing of the $1/T_1$ in the zero-temperature limits.

We have also measured LF-μSR spectra for $T = 0.1$ K at different magnetic fields, applied along the direction of incident muons, as shown in Fig. 6(a). It is evident that with the application of 11.1 mT, the muon relaxation is suppressed and the asymmetry becomes flat with long-time asymmetry being recovered. The curves were fitted using the exponential function $A_0 e^{(-\lambda_{LF}t)}$, which suggests the homogeneous distribution of the muons inside the sample. A similar description is reported for the homogeneous system YbRh$_2$Si$_2$ [75] and the doped compound YbNi$_4$(P$_{1-x}$As$_x$)$_2$ [70]. Figure 6(b) shows the field variation of the relaxation rate λ_{LF} obtained from the LF fits, which decreases rapidly with increasing magnetic field. The field variation of λ_{LF} gives information regarding the spin auto-correlation time τ_C, which is estimated using the Redfield formalism [76]:

$$\lambda_{LF} = \frac{2(\gamma_\mu H_{loc})^2 \tau_C}{\left[1 + (\gamma_\mu H_{LF} \tau_C)^2\right]}. \qquad (3)$$

Here, H_{loc} is the time-varying local magnetic field at the muon site due to the fluctuation of neighboring Ce moments. The best fit to the data using Eq. (3) [the solid red line in Fig. 6(b)] yields $\tau_C \approx 5.9 \times 10^{-6}$ s, indicating very slow critical fluctuations. The value of the correlation time is nearly the same as that obtained for the homogeneous system [70]. Also, the field dependence of the relaxation rate λ_{LF} follows a power-law behavior, $\lambda_{LF}(H) \sim H^{-\gamma}$ with $\gamma \sim 0.97(1)$ [77] [the black dotted line in Fig. 6(b)]. This value of γ is consistent with the exponent γ obtained from the time-field scaling plots (described in Sec. III E), where the time-field scaling relation implies $\lambda_{LF}(H) \propto H^{-\gamma}$.
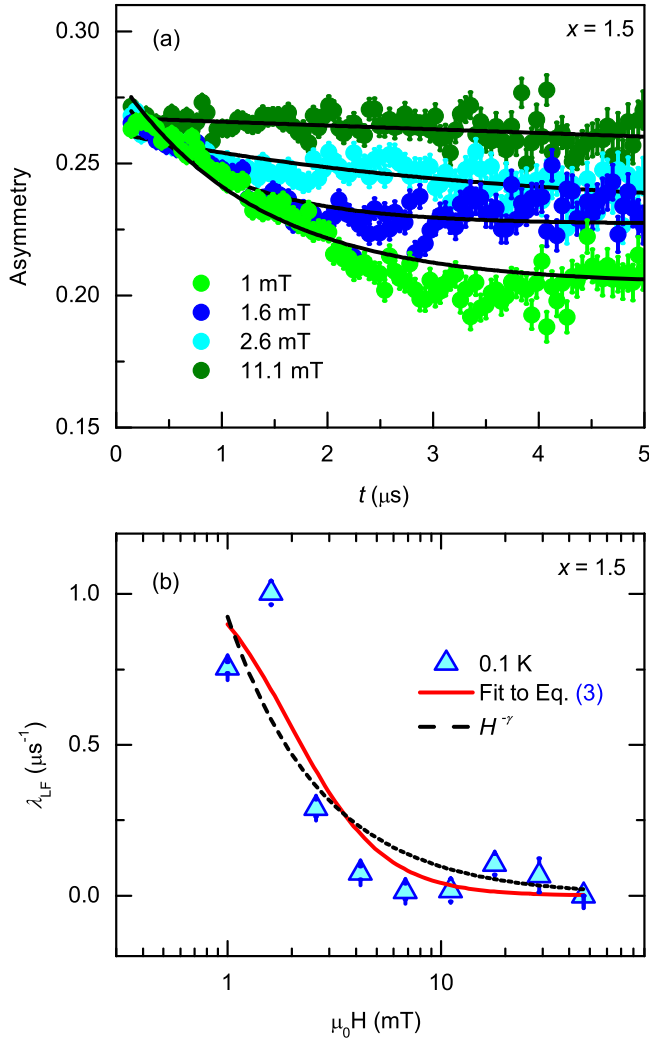
FIG. 6. (a) LF-μSR spectra for 0.1 K at selected fields; the solid lines are the fits as described in the text. (b) Field dependence of the relaxation rate λ_{LF}, where the solid red line is the fit to Eq. (3) and the black dotted line shows the power-law fit.
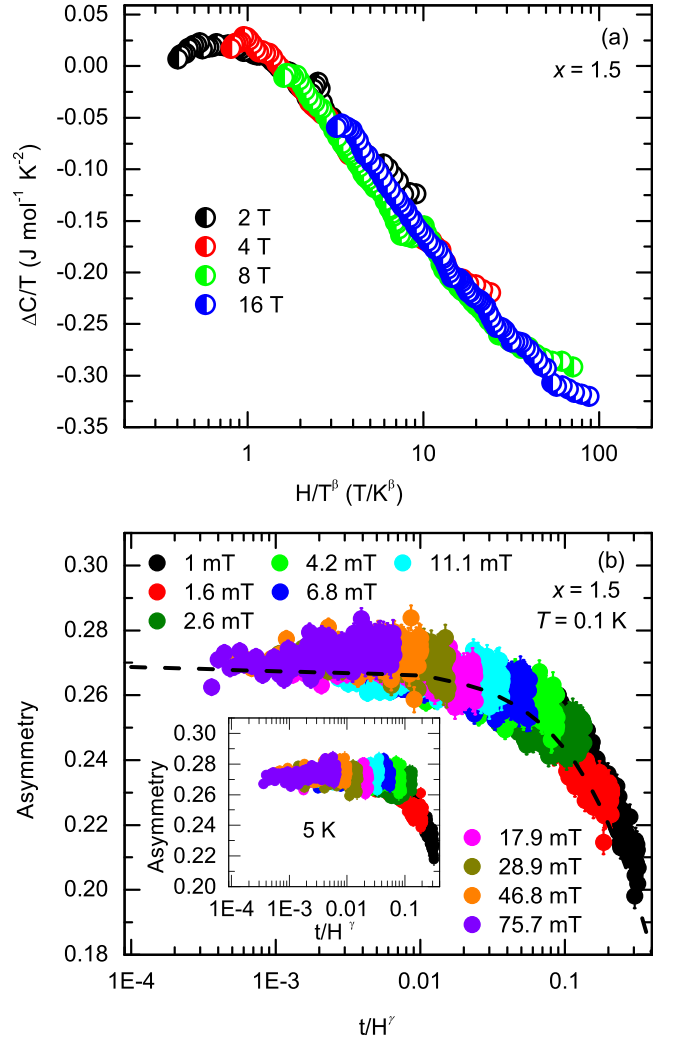

FIG. 7. (a) Scaling collapse of the heat capacity curve measured at different constant fields. (b) Time-field scaling of LF-μSR spectra at 0.1 K, where the dashed line is fit to the relation as described in the main text. Inset shows a time-field scaling curve at 5 K.

E. Universal scaling

The system near a QCP shows a critical behavior, and the thermodynamical properties like heat capacity and magnetization should obey a universal scaling behavior [78,79]. Figure 7(a) shows the temperature-field scaling of the heat capacity data for $x_C \sim 1.5$. All the curves collapse onto a single universal curve following the scaling function $C(H, T)/T - C(0, T)/T = g(HT^{-\beta})$ with the exponent $\beta \sim 1.1 \pm 0.1$. This is in line with our magnetization scaling [4] and further confirms that the system is at a QCP. Similar scaling analyses with a similar choice of exponent β are observed for stoichiometric CeNi$_2$Ge$_2$ [80] and YbRh$_2$Si$_2$ [81] compounds.

Further, the time-field (t/H^γ) scaling of the 0.1 K data measured at different longitudinal fields is shown in the main panel of Fig. 7(b), while the inset shows the time-field scaling of the 5 K data. The time-field scaling of LF-μSR data is considered a unique property for the systems showing nFL behavior. The exponent γ provides us with information

regarding the spin-spin dynamical autocorrelation function $q(t)$ [68,76,82]. The universal behavior is obtained with the choice of $\gamma \sim 0.9 \pm 0.1$ for both 0.1 and 5 K curves, where all the data scale well. The information regarding $q(t)$ can be obtained using the time-field scaling relation because $q(t)$ is theoretically predicted to exhibit a power-law correlation $q(t) = ct^{-\alpha}$ with $\gamma = 1 - \alpha < 1$ and stretched exponential correlation $q(t) = c \, e^{(-\lambda t)^\beta}$ for $\gamma = 1 + \beta > 1$ [77]. Thus, our value of the scaling exponent $\gamma \sim 0.9 \pm 0.1$ (which is close to 1) indicates that $q(t)$ can be approximated either by a power law or a stretched exponential. The value of exponent γ obtained from the time-field scaling relation is consistent with γ obtained from the power-law behavior $\lambda_{LF}(H) \propto H^{-\gamma}$ [Fig. 6(b)], which suggests long spin-spin correlation times and slow magnetic spin fluctuations as expected near the critical region.

Our observed value of γ is close to the values reported for the systems showing QCP, such as Sm$_{1-x}$La$_x$NiC$_2$ ($x = 0.92$) [83], CePd$_{0.15}$Rh$_{0.85}$ [36], and YbRh$_2$Si$_2$ [68]. In our case, γ is
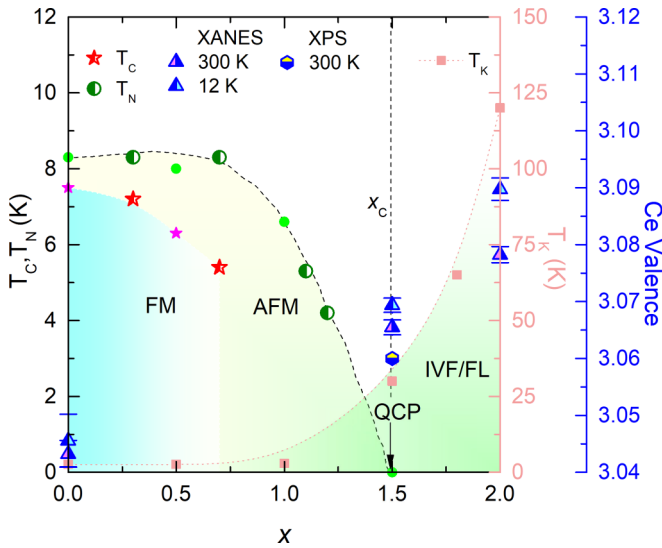
FIG. 8. T-x phase diagram of CeRu$_{2-x}$Co$_x$Ge$_2$ including the results of $C(T)$, XANES, and XPS measurements for different x from the present study. Some data points (green solid circles, magenta stars, and T_K) are taken from Ref. [4]. The right scale in blue shows the valence of the Ce ion.

independent of temperature, as the value of the exponent γ is similar for 0.1 and 5 K data, which indicates that the origin of these slow fluctuations is quantum rather than thermal [77]. In contrast, the temperature dependence of γ is usually observed for the glassy system, e.g., AgMn, where γ increases as the temperature approaches the glass transition temperature [82]. The dashed line in the main panel of Fig. 7(b) is the fit using stretched-exponential relation $e^{(-\lambda_{LF}t)^\beta}$ with $\beta \sim 1.15$. The closeness of the exponent β to unity implies that there is an exponential relaxation throughout the sample, which further confirms that the system exhibits homogeneous spin fluctuations [70].

IV. DISCUSSION

The above findings for the critical concentration suggest the coinciding spin and valence fluctuations at a $T = 0$ K QCP. Nonetheless, a complete insight into the interplay of the spin and valence fluctuations could be envisaged from the T-x phase diagram (see Fig. 8). The T_C and T_N values obtained from the heat capacity measurements for our new compositions, $x = 0.3$, 0.7, 1.1, and 1.2, smoothly traverse the Doniach phase diagram and show a complete suppression of T_N near $x_C \sim 1.5$, resulting in an AFM QCP. The results of our low-temperature heat capacity and the muon depolarization rate λ_{ZF} for $x_C \sim 1.5$ further confirm an AFM QCP consistent with the spin fluctuation theory of Moriya [14]. It should be noted that the description of spin fluctuation theory is generally valid for the $3d$ itinerant systems [15]. Surprisingly, a similar description of the heat capacity using spin fluctuation theory has been obtained for Ce$_{1-x}$La$_x$Ru$_2$Si$_2$, CeCu$_{5.8}$Au$_{0.2}$, and YbCu$_{3.5}$Al$_{1.5}$ in the case of $4f$ localized systems [84–86]. Additionally, the temperature-field and time-field scaling of

the heat capacity and LF-μSR, respectively, suggest the importance of slow and long ranged critical fluctuations near an AFM QCP.

Nonetheless, the temperature-dependent XANES and XPS results for the present case suggest the role of incipient valence fluctuations for $x_C \sim 1.5$ due to its proximity to the IVF compound CeCo$_2$Ge$_2$ [32,33]. This is also supported by the muon depolarization rate λ_{ZF} for $x_C \sim 1.5$, which could be described using the VF QCP below 0.2 K [72,73]. The survival of valence fluctuations down to the lowest temperature further validates our previous resistivity and magnetization results in favor of VF QCP [4]. An increase in the Ce valence with x indicates the strengthening of the $4f$-conduction electron hybridization, as demonstrated by an increase in Kondo temperature T_K [4].

In addition, the role of disorder inherent to doping presents an important trait for the study of the QPTs. For example, the quantum Griffiths phase as a result of doping-induced disorder was recently reviewed in Ce(Cu$_{1-x}$Co$_x$)$_2$Ge$_2$ [87]. Another study proposed similar disorder-induced clusters in Ce(Fe$_{0.76}$Ru$_{0.24}$)$_2$Ge$_2$, formed as a result of the distribution of local Kondo screening temperatures [88]. In general, disorder-driven theories such as the Griffiths phase model or Kondo disorder model can produce a distribution of local fluctuation rates. However, the cooperative phenomena in CeRu$_{2-x}$Co$_x$Ge$_2$ resulting from time-field scaling behavior and the homogeneous relaxation of the μSR depolarization rate contradict the role of various correlation times, implying that the disorder has a minimal contribution to the current system.

V. CONCLUSIONS

The Ce L_{III} edge XANES profile for CeRu$_{2-x}$Co$_x$Ge$_2$ ($x = 0$, 1.5, and 2) confirms the valence fluctuating state for $x \geqslant 1.5$. The XPS results further verify the noninteger valence for the critical concentration, $x_C \sim 1.5$. However, the AFM QCP is strongly supported by the lack of long-range magnetic ordering at $x_C \sim 1.5$, as confirmed by ZF-μSR and heat capacity measurements down to 50 mK. The temperature-field and time-field scaling analyses of heat capacity and LF-μSR data, respectively, confirm the significance of critical and cooperative spin fluctuations around this AFM QCP. Moreover, the behavior of $\lambda_{ZF}(T)$ strongly suggests the role of valence fluctuations surviving down to the lowest measured temperatures in accordance with the VF QCP. A substantial hybridization of the $4f$ and conduction electrons suggests the simultaneous interplay of the spin and valence fluctuations driving the quantum criticality in CeRu$_{2-x}$Co$_x$Ge$_2$.

[1] F. Steglich, J. Aarts, C. D. Bredl, W. Lieke, D. Meschede, W. Franz, and H. Schäfer, Phys. Rev. Lett. **43**, 1892 (1979).

[2] J. M. Lawrence, P. S. Riseborough, and R. D. Parks, Rep. Prog. Phys. **44**, 1 (1981).

[3] P. Wachter, in *Handbook on the Physics and Chemistry of Rare Earths*, edited by K. A. Gschneider, Jr., L. Eyring, G. H. Lander, and G. R. Choppin (Elsevier, New York, 1994), Vol. 19, pp. 177–382.

[4] S. Pandey, V. Siruguri, and R. Rawat, Phys. Rev. B **98**, 155129 (2018).

[5] R. Rawat and V. G. Sathe, J. Phys.: Condens. Matter **17**, 313 (2005).

[6] M. B. Fontes, M. A. Continentino, S. L. Bud'ko, M. El-Massalami, L. C. Sampaio, A. P. Guimarães, E. Baggio-Saitovitch, M. F. Hundley, and A. Lacerda, Phys. Rev. B **53**, 11678 (1996).

[7] E. V. Sampathkumaran and R. Vijayaraghavan, Phys. Rev. Lett. **56**, 2861 (1986).

[8] S. Doniach, Physica B+C **91**, 231 (1977).

[9] P. Gegenwart, Q. Si, and F. Steglich, Nat. Phys. **4**, 186 (2008).

[10] Q. Si and F. Steglich, Science **329**, 1161 (2010).

[11] P. Coleman and A. J. Schofield, Nature (London) **433**, 226 (2005).

[12] T. Graf, J. D. Thompson, M. F. Hundley, R. Movshovich, Z. Fisk, D. Mandrus, R. A. Fisher, and N. E. Phillips, Phys. Rev. Lett. **78**, 3769 (1997).

[13] H. v. Löhneysen, A. Rosch, M. Vojta, and P. Wölfle, Rev. Mod. Phys. **79**, 1015 (2007).

[14] T. Moriya and T. Takimoto, J. Phys. Soc. Jpn. **64**, 960 (1995).

[15] G. R. Stewart, Rev. Mod. Phys. **73**, 797 (2001).

[16] O. O. Bernal, D. E. MacLaughlin, H. G. Lukefahr, and B. Andraka, Phys. Rev. Lett. **75**, 2023 (1995).

[17] A. H. Castro Neto, G. Castilla, and B. A. Jones, Phys. Rev. Lett. **81**, 3531 (1998).

[18] K. Yamamoto, H. Yamaoka, N. Tsujii, A. M. Vlaicu, H. Oohashi, S. Sakakura, T. Tochio, Y. Ito, A. Chainani, and S. Shin, J. Phys. Soc. Jpn. **76**, 124705 (2007).

[19] Q. Si, S. Rabello, K. Ingersent, and J. L. Smith, Nature (London) **413**, 804 (2001).

[20] C. Mazumdar, R. Nagarajan, C. Godart, L. C. Gupta, B. D. Padalia, and R. Vijayaraghavan, J. Appl. Phys. **79**, 6347 (1996).

[21] R. Gumeniuk, K. O. Kvashnina, W. Schnelle, M. Nicklas, H. Borrmann, H. Rosner, Y. Skourski, A. A. Tsirlin, A. Leithe-Jasper, and Yu Grin, J. Phys.: Condens. Matter **23**, 465601 (2011).

[22] R. Feyerherm, E. Dudzik, S. Valencia, J. A. Mydosh, Y.-K. Huang, W. Hermes, and R. Pöttgen, Phys. Rev. B **85**, 085120 (2012).

[23] H. Yamaoka, Y. Ikeda, I. Jarrige, N. Tsujii, Y. Zekko, Y. Yamamoto, J. Mizuki, J.-F. Lin, N. Hiraoka, H. Ishii, K. D. Tsuei, T. C. Kobayashi, F. Honda, and Y. Onuki, Phys. Rev. Lett. **113**, 086403 (2014).

[24] M. Croft, R. Neifeld, C. U. Segre, S. Raaen, and R. D. Parks, Phys. Rev. B **30**, 4164 (1984).

[25] R. A. Neifeld, M. Croft, T. Mihalisin, C. U. Segre, M. Madigan, M. S. Torikachvili, M. B. Maple, and L. E. DeLong, Phys. Rev. B **32**, 6928 (1985).

[26] Y. Onishi and K. Miyake, J. Phys. Soc. Jpn. **69**, 3955 (2000).

[27] J.-P. Rueff, S. Raymond, M. Taguchi, M. Sikora, J.-P. Itié, F. Baudelet, D. Braithwaite, G. Knebel, and D. Jaccard, Phys. Rev. Lett. **106**, 186405 (2011).

[28] M. Okawa, M. Matsunami, K. Ishizaka, R. Eguchi, M. Taguchi, A. Chainani, Y. Takata, M. Yabashi, K. Tamasaku, Y. Nishino, T. Ishikawa, K. Kuga, N. Horie, S. Nakatsuji, and S. Shin, Phys. Rev. Lett. **104**, 247201 (2010).

[29] S. Nakatsuji, K. Kuga, Y. Machida, T. Tayama, T. Sakakibara, Y. Karaki, H. Ishimoto, S. Yonezawa, Y. Maeno, E. Pearson, G. G. Lonzarich, L. Balicas, H. Lee, and Z. Fisk, Nat. Phys. **4**, 603 (2008).

[30] H. Wilhelm and D. Jaccard, Solid State Commun. **106**, 239 (1998).

[31] A. Loidl, K. Knorr, G. Knopp, A. Krimmel, R. Caspary, A. Böhm, G. Sparn, C. Geibel, F. Steglich, and A. P. Murani, Phys. Rev. B **46**, 9341 (1992).

[32] H. Fujii, E. Ueda, Y. Uwatoko, and T. Shigeoka, J. Magn. Magn. Mater. **76-77**, 179 (1988).

[33] A. P. Pikul, M. Pasturel, P. Wisniewski, A. Soudé, O. Tougait, H. Noël, and D. Kaczorowski, Intermetallics **53**, 40 (2014).

[34] A. Yaouanc and P. Dalmas de Reotier, *Muon Spin Rotation, Relaxation, and Resonance: Applications to Condensed Matter* (Oxford University Press, New York, 2011).

[35] A. Amato, Rev. Mod. Phys. **69**, 1119 (1997).

[36] D. T. Adroja, A. D. Hillier, J.-G. Park, W. Kockelmann, K. A. McEwen, B. D. Rainford, K.-H. Jang, C. Geibel, and T. Takabatake, Phys. Rev. B **78**, 014412 (2008).

[37] A. K. Poswal, A. Agrawal, A. K. Yadav, C. Nayak, S. Basu, S. R. Kane, C. K. Garg, D. Bhattacharyya, S. N. Jha, and N. K. Sahoo, AIP Conf. Proc. **1591**, 649 (2014).

[38] G. Liang, M. Croft, D. C. Johnston, N. Anbalagan, and T. Mihalisin, Phys. Rev. B **38**, 5302 (1988).

[39] D. Wohlleben, in *Valence Fluctuations in Solids*, edited by L. M. Falicov, W. Hanke, and M. B. Maple (North-Holland, Amsterdam, 1981), pp. 1–11.

[40] B. Buffat, B. Chevalier, M. H. Tuilier, B. Lloret, and J. Etourneau, Solid State Commun. **59**, 17 (1986).

[41] E. V. Sampathkumaran, G. Kalkowski, C. Laubschat, G. Kaindl, M. Domke, G. Schmiester, and G. Wortmann, J. Magn. Magn. Mater. **47-48**, 212 (1985).

[42] D. Gignoux, D. Schmitt, M. Zerguine, and A. P. Murani, J. Magn. Magn. Mater. **76-77**, 401 (1988).

[43] H. Schneider, Z. Kletowski, F. Oster, and D. Wohlleben, Solid State Commun. **48**, 1093 (1983).

[44] J. Röhler, J. Magn. Magn. Mater. **47-48**, 175 (1985).

[45] D. Kaczorowski, A. P. Pikul, U. Burkhardt, M. Schmidt, A. Ślebarski, A. Szajek, M. Werwiński, and Y. Grin, J. Phys.: Condens. Matter **22**, 215601 (2010).

[46] U. B. Paramanik, U. Burkhardt Anupam, R. Prasad, C. Geibel, and Z. Hossain, J. Alloys Compd. **580**, 435 (2013).

[47] O. Niehaus, P. M. Abdala, R. St Touzani, B. P. T. Fokwa, and R. Pottgen, Solid State Sci. **40**, 36 (2015).

[48] A. L. Cornelius, J. M. Lawrence, J. L. Sarrao, Z. Fisk, M. F. Hundley, G. H. Kwei, J. D. Thompson, C. H. Booth, and F. Bridges, Phys. Rev. B **56**, 7993 (1997).

[49] J. L. Sarrao, C. D. Immer, Z. Fisk, C. H. Booth, E. Figueroa, J. M. Lawrence, R. Modler, A. L. Cornelius, M. F. Hundley, G. H. Kwei, J. D. Thompson, and F. Bridges, Phys. Rev. B **59**, 6855 (1999).

[50] Y. H. Matsuda, T. Inami, K. Ohwada, Y. Murata, H. Nojiri, Y. Murakami, H. Ohta, W. Zhang, and K. Yoshimura, J. Phys. Soc. Jpn. **76**, 034702 (2007).

[51] S. Watanabe and K. Miyake, J. Phys.: Condens. Matter **23**, 094217 (2011).

[52] S. Watanabe, A. Tsuruta, K. Miyake, and J. Flouquet, J. Phys. Soc. Jpn. **78**, 104706 (2009).

[53] C. Tien, L. Y. Jang, C. Y. Kuo, J. J. Lu, and S. W. Feng, J. Phys.: Condens. Matter **12**, 8983 (2000).

[54] S. Majumdar and E. V. Sampathkumaran, Phys. Rev. B **62**, 8959 (2000).

[55] M. B. Gamza, R. Gumeniuk, U. Burkhardt, W. Schnelle, H. Rosner, A. Leithe-Jasper, and A. Slebarski, Phys. Rev. B **95**, 165142 (2017).

[56] S. Doniach and M. Sunjic, J. Phys. C **3**, 285 (1970).

[57] J. C. Fuggle, F. U. Hillebrecht, Z. Zolnierek, R. Lässer, Ch. Freiburg, O. Gunnarsson, and K. Schönhammer, Phys. Rev. B **27**, 7330 (1983).

[58] O. Gunnarsson and K. Schönhammer, Phys. Rev. B **28**, 4315 (1983).

[59] E. Wuilloud, H. R. Moser, W. D. Schneider, and Y. Baer, Phys. Rev. B **28**, 7354 (1983).

[60] A. Slebarski, T. Zawada, J. Spałek, and A. Jezierski, Phys. Rev. B **70**, 235112 (2004).

[61] A. Ślebarski, J. Deniszczyk, and D. Kaczorowski, Materials **13**, 2377 (2020).

[62] A. Ślebarski and J. Deniszczyk, J. Magn. Magn. Mater. **563**, 169997 (2022).

[63] M. B. Gamza, W. Schnelle, A. Ślebarski, U. Burkhardt, R. Gumeniuk, and H. Rosner, J. Phys.: Condens. Matter **20**, 395208 (2008).

[64] A. P. Pikul, D. Kaczorowski, Z. Gajek, J. Stepien-Damm, A. Slebarski, M. Werwinski, and A. Szajek, Phys. Rev. B **81**, 174408 (2010).

[65] V. Eyert, E.-W. Scheidt, W. Scherer, W. Hermes, and R. Pöttgen, Phys. Rev. B **78**, 214420 (2008).

[66] K. An, T. Sakakibara, R. Settai, Y. Onuki, M. Hiragi, M. Ichioka, and K. Machida, Phys. Rev. Lett. **104**, 037002 (2010).

[67] R. Kubo and T. Toyabe, in *Magnetic Resonance and Relaxation*, edited by R. Blinc (North-Holland, Amsterdam, 1967), pp. 810–823.

[68] R. S. Hayano, Y. J. Uemura, J. Imazato, N. Nishida, T. Yamazaki, and R. Kubo, Phys. Rev. B **20**, 850 (1979).

[69] K. Huang, C. Tan, J. Zhang, Z. Ding, D. E. MacLaughlin, O. O. Bernal, P.-C. Ho, C. Baines, L. S. Wu, M. C. Aronson, and L. Shu, Phys. Rev. B **97**, 155110 (2018).

[70] R. Sarkar, J. Spehling, P. Materne, H. Luetkens, C. Baines, M. Brando, C. Krellner, and H. H. Klauss, Phys. Rev. B **95**, 121111(R) (2017).

[71] P. Carretta, R. Pasero, M. Giovannini, and C. Baines, Phys. Rev. B **79**, 020401(R) (2009).

[72] K. Miyake and S. Watanabe, Phys. Rev. B **98**, 075125 (2018).

[73] K. Miyake and S. Watanabe, J. Phys. Soc. Jpn. **83**, 061006 (2014).

[74] D. E. MacLaughlin, K. Kuga, L. Shu, O. O. Bernal, P.-C. Ho, S. Nakatsuji, K. Huang, Z. F. Ding, C. Tan, and J. Zhang, Phys. Rev. B **93**, 214421 (2016).

[75] K. Ishida, D. E. MacLaughlin, B.-L. Young, K. Okamoto, Y. Kawasaki, Y. Kitaoka, G. J. Nieuwenhuys, R. H. Heffner, O. O. Bernal, W. Higemoto, A. Koda, R. Kadono, O. Trovarelli, C. Geibel, and F. Steglich, Phys. Rev. B **68**, 184401 (2003).

[76] Y. J. Uemura, T. Yamazaki, D. R. Harshman, M. Senba, and E. J. Ansaldo, Phys. Rev. B **31**, 546 (1985).

[77] D. E. MacLaughlin, R. H. Heffner, O. O. Bernal, K. Ishida, J. E. Sonier, G. J. Nieuwenhuys, M. B. Maple, and G. R. Stewart, J. Phys.: Condens. Matter **16**, S4479 (2004).

[78] B. Andraka and A. M. Tsvelik, Phys. Rev. Lett. **67**, 2886 (1991).

[79] A. M. Tsvelik and M. Reizer, Phys. Rev. B **48**, 9887 (1993).

[80] S. Koerner, E.-W. Scheidt, T. Schreiner, K. Heuser, and G. R. Stewart, J. Low Temp. Phys. **119**, 147 (2000).

[81] O. Trovarelli, C. Geibel, S. Mederle, C. Langhammer, F. M. Grosche, P. Gegenwart, M. Lang, G. Sparn, and F. Steglich, Phys. Rev. Lett. **85**, 626 (2000).

[82] A. Keren, P. Mendels, I. A. Campbell, and J. Lord, Phys. Rev. Lett. **77**, 1386 (1996).

[83] W. Lee, S. Lee, K. -Y. Choi, K. -J. Lee, B. -J. Kim, B. J. Suh, B. Shin, and T. Park, Phys. Rev. B **96**, 224433 (2017).

[84] S. Kambe, S. Raymond, H. Suderow, J. Mc Donough, B. Fak, L. P. Regnault, R. Calemczuk, and J. Flouquet, Phys. B (Amsterdam, Neth.) **223-224**, 135 (1996).

[85] H. v. Löhneysen, C. Pfleiderer, T. Pietrus, O. Stockert, and B. Will, Phys. Rev. B **63**, 134411 (2001).

[86] C. Seuring, E.-W. Scheidt, E. Bauer, and G. R. Stewart, J. Low Temp. Phys. **123**, 25 (2001).

[87] R. Tripathi, D. Das, P. K. Biswas, D. T. Adroja, A. D. Hillier, and Z. Hossain, Phys. Rev. B **99**, 224424 (2019).

[88] W. Montfrooij, T. Heitmann, Y. Qiu, S. Watson, R. Erwin, W. Chen, Y. Zhao, M. Aronson, Y. Huang, and A. de Visser, Phys. Rev. B **99**, 195113 (2019).